New Reconstruction Method for Needle Contrast Optimization in B-Mode Ultrasound Image by Extracting RF Signal Parameters in Frequency Domain

Hesty Susanti, Suprijanto* & Deddy Kurniadi

Instrumentation and Control Research Group, Faculty of Industrial Technology, Institut Teknologi Bandung, Jalan Ganesha No. 10, Bandung 40132, Indonesia
*E-mail: supri@tf.itb.ac.id

Highlights:

- The result suggests that the reconstruction of needle images should be derived from the maximum power spectral density and the energy spectral density to optimize the contrast of the needle in B-mode ultrasound images.
- The effect of resonance scattering around critical incident angles is observed more clearly at maximum power spectral density and energy spectral density than in the signal envelope.
- The fractional bandwidth of the backscattered pressure field from the resonance scattering model is relatively optimal at 40% to 100% bandwidth.

Abstract. Ultrasound-guided needle insertion has become standard in medical interventional procedures. Regardless of its advantages, it still has crucial problems related to needle visibility. Some technical factors affect the visibility with non-linear characteristic, i.e. frequency, insertion angle and depth. Here, backscattered signal parameters from measurement were compared to a simulation of a resonance scattering model. Raw radio frequency (RF) data were reconstructed with a new method to represent unique information on total backpropagation from the needle, which consists of non-resonance and resonance scattering components. The result suggests that reconstruction of the needle in B-mode images should be derived from the maximum power spectral density and the energy spectral density to optimize the contrast of the needle. In measurements with the center frequency at 1.87 MHz, the effect of resonance scattering on the total backpropagation around critical angles could be observed more clearly with this method than with standard reconstruction based on the signal envelope. The simulation showed that the fractional bandwidth of the spectrum of the backscattered pressure field centered at 1.87 MHz was relatively optimal at 40% to 100%. So that the simulation of the resonance scattering model can be used to predict the backscattered response from the needle, it must be able to confirm it to the real conditions of RF data with random characteristics. Therefore, extraction of the backscattered pressure field in a simulation with fractional bandwidth should be a concern.

Received November 15th, 2019, 1st Revision May 4th, 2020, 2nd Revision May 27th, 2020, Accepted for publication June 17th, 2020.

DOI: 10.5614/j.eng.technol.sci.2020.52.4.5

Keywords: *energy spectral density; needle visibility; power spectral density; resonance scattering; RF data processing; signal envelope; ultrasound.*

1 Introduction

The application of ultrasound imaging to guide needle insertion has become standard in medical interventional procedures. It comes with some advantages compared to other medical imaging modalities in terms of the absence of ionization risk [1], the small size of the equipment [2], and the flexibility of the imaging planes [3]. At the same time, ultrasound-guided needle insertion still has crucial problems in terms of needle visibility. Enhancement of needle visibility could improve the quality of the interventional procedure, e.g. avoiding the risk of insertion errors, reducing the time required and reducing patient morbidity.

It has been reported that targeting in percutaneous interventions can be complicated by poor needle visibility [4]. Other studies investigated similar problems associated with poor needle visibility [5-10]. Needle visibility is also influenced by the type of needle, either echogenic or non-echogenic, which makes the visibility problem more complicated [11].

The standard technique for reconstruction of B-mode ultrasound images from raw radio frequency (RF) data in clinical applications is derived on the basis of envelope detection. This technique is complemented by a series of post-processing steps mainly used to reconstruct images of biological tissue, balancing between information content and visual appeal, e.g. contrast, spatial resolution, and perception of changes in brightness. This standard reconstruction method is well established in representing images of biological tissue in clinical applications, e.g. ob-gyn, cardiac, abdominal, and lung ultrasound which has recently been found to be quite promising for early detection of pneumonia of COVID-19 [12-14]. Despite its advantages, this reconstruction method is not reliable for images of non-biological objects, such as needles.

In needle images, visibility tends to be varied in standard B-mode ultrasound images. Poorer needle visibility is expected at larger insertion angles due to the larger incident angle of the ultrasound beam to the needle, but it reappears for larger incident angles around 50-70° [15, 16]. For example, in Figure 1, at 40°, the needle shaft can be imaged fully, but at 50° the beginning part of the needle shaft disappears. This indicates a unique behavior of needle visibility. It cannot be explained simply by common acoustic reflection, assuming the needle as a specular surface. Apparently, the standard technique of B-mode ultrasound image reconstruction does not fully accommodate the unique characteristics of acoustic reflection from the needle as a specular surface. Some technical factors affect it, e.g. insertion angle and ultrasound frequency, but no linearity has been found.

The previous studies by Dencks, *et al.* [15, 16] explained that the distinctive character of the acoustic reflection from needles, in addition to specular reflection, is caused by resonance scattering, especially around critical incident angles.

In this research, the backscattered signal parameters obtained from measurement were compared to an acoustic backscattering model based on the resonance scattering model from a simulation. In this case, the resonance scattering model was taken as the standard reference due to its idealized assumptions. Raw RF data from the measurement were processed in the time domain and the frequency domain to find the most suitable reconstruction method to represent the unique information of the total backpropagation from the needle compared to the resonance scattering model. This new reconstruction method was developed to optimize the contrast of the needle in B-mode ultrasound images, which in this specific case is caused by non-resonance and resonance scattering components.

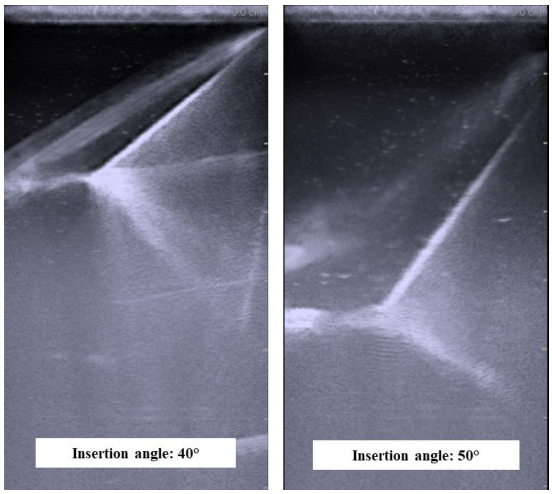

Figure 1 Needle visibility tends to vary at various insertion angles in standard B-mode ultrasound images.

This paper is divided into 7 sections. After the introduction of the topic (Section 1), the explanations are divided into 3 categories, i.e. measurement, modeling and simulation, and the comparison between them. Radio frequency (RF) data measurement is explained in Section 2, followed by the backscattered signal parameters from the measurement (Section 3). The modeling and simulation of resonance scattering are explained in Section 4, followed by a comparison between the resonance scattering model from simulation and the backscattered parameters from measurement (Section 5). The result and discussion are explained elaborately in Section 6, followed by the conclusion in Section 7.

2 Radio Frequency (RF) Data Measurement

Measurements were performed through ultrasonic spectroscopy by obtaining raw RF data per single A-mode scan-line. RF signals arriving first at the transducer's element (receiver) were assumed to be in raw form, representing the backscattered pressure field [15]. The effect of beamforming was excluded in the measurement to purely observe the effect of wave phenomena. One 22G spinal needle (Zhejiang Shendasiao Medical Instrument, China; outer radius a = 0.72 mm, inner radius b = 0.41 mm) was measured with a couple of single element immersion transducers (Sonatest IMR3750, Sonatest, Milton Keynes, United Kingdom), consisting of one transmitter and one receiver.

The gauge number (G) expresses the size of the needle's diameter, the smaller the gauge number the larger the needle's diameter. Demineralized water (ρ = 997 kg/m^3) in an acrylic water tank was used as background medium. One-cm thick vilt wool was placed on the bottom of the tank to prevent reflection from the tank's bottom wall. Before measurement, the demineralized water was degassed by pumping out dissolved air bubbles with a vacuum pump. These steps were performed to create an homogenous and anechoic environment as background medium for the measurements. The needle was placed under the water surface within the far-field zone of the transducer, in-plane with the transducer at angles varied in the range of 0 to 45° (resolution = 5°). With the experiment set up, the optimal transmit frequency was set at 1.87 MHz by driving the transducer with the pulser. The retrieved raw RF data from the transducer were sampled and recorded with an oscilloscope (RIGOL DS1052E, RIGOL Technologies, Beijing China) with a sampling frequency of 100 MHz to be processed later by a computer. The measurement setup is shown in Figure 2.

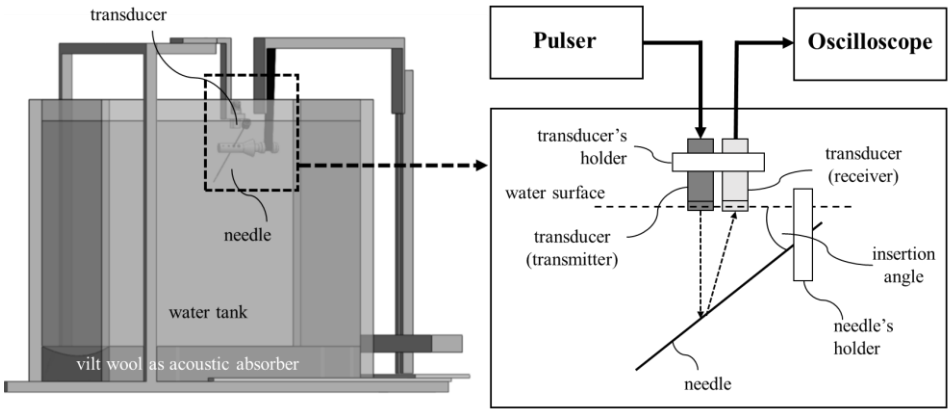

Figure 2 The RF data measurement setup.

3 Backscattered Signal Parameters

The recorded raw RF data from the oscilloscope were processed in a computer with MATLAB 2018b (Mathworks, Natick, MA, United States). Basically, these processes can be divided into two domains, the time domain and the frequency domain. The signal parameter in the time domain represents the standard method of B-mode image reconstruction by extracting the signal envelope, while the signal parameters in the frequency domain were the new proposed parameters for B-mode needle image reconstruction in this research. These signal parameters in the time and the frequency domain were later compared to the resonance scattering model as standard reference.

3.1 Backscattered Signal Parameter in the Time Domain

In reconstruction of standard B-mode ultrasound images, the signal received by each transducer's element represented by raw RF data are proportional to the total backpropagation or the backscattered pressure field. The raw RF data can be represented as an analytic signal in complex form as in Eq. (1):

$$y(t) = A(t).cos[2\pi f_C t + \varphi(t)] + i.A(t)sin[2\pi f_C t + \varphi(t)] \quad (1)$$

An analytic signal is a modulated signal that consists of positive and negative frequency components that are deemed due to symmetry [17,18]. $A(t)$ represents the amplitude function, f_C is the center frequency and $\varphi(t)$ is the phase function. Eq. (1) can be written in the form such in Eq. (2) as follows:

$$y(t) = A(t)e^{[2\pi f_C t + \varphi(t)]} = m(t)e^{i2\pi f_C t} \quad (2)$$

where $m(t) = A(t)e^{i\varphi(t)}$ represents the complex envelope, combining the amplitude and phase information of the signal. After this step, the signal is demodulated to remove the oscillatory carrier part of the signal, where the original information containing the signal is separated from the modulated carrier wave that is needed to convey the signal pulse. This is performed in each scan line independently [19]. This step is commonly called envelope detection, which is done by taking the absolute value of the analytic signal, resulting in the signal envelope as in Eq. (3) as follows:

$$y_{envelope} = |y(t)| = \sqrt{x(t)^2 + x_H(t)^2} \quad (3)$$

where $x_H(t)$ represents the Hilbert transformed signal of $x(t)$, which is the real component of $y(t)$ [17, 20, 18]. Technically, raw RF data are converted into a signal envelope by returning the upper and lower peak envelopes of the raw signal. The envelopes are determined using spline interpolation over local maxima separated by at least np peak separation parameter samples. This whole process is shown in Figure 3.

The signal envelope is the basis for further signal processing, i.e. log-compression, scan-conversion, and B-mode filtering, like in the generation of standard B-mode ultrasound images in clinical applications. B-mode imagery is affected by non-linear post-processing steps, such as log-compression and other proprietary filter algorithms that change the statistics character of the signal for reasons of improved visual appeal [19].

In the signal acquisition process, the modulated signal represents the raw RF data in each scan-line retrieved from the transducer can be written as in Eq. (4) as follows [20]:

$$x(t) = Re\big(y(t)\big) = A(t).cos[2\pi f_C t + \varphi(t)] \tag{4}$$

$x(t)$ is only the real component of RF data $y(t)$ in Eqs. (1) and (2). In this specific case of needle image reconstruction, compared to Eq. (4), $A(t)$ here represents the scattering coefficient, g_n. It consists of the superposition of all the phases and amplitudes from each scattering reflection from the needle, which contains resonance and non-resonance components.

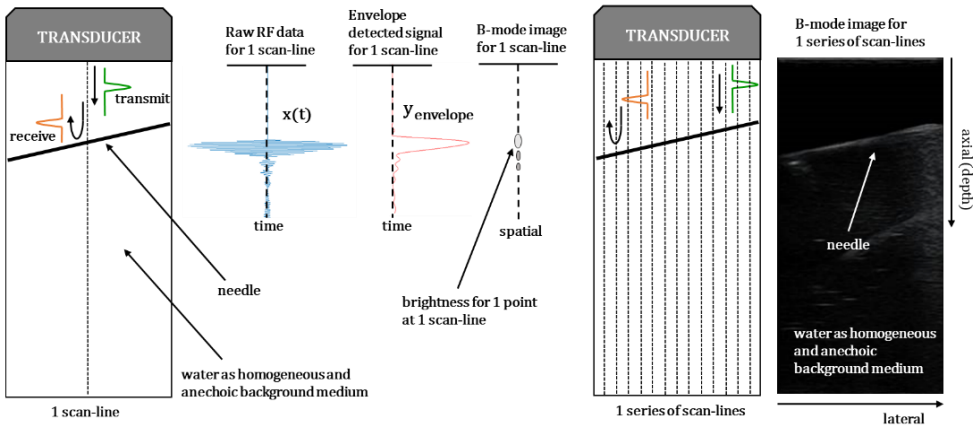

Figure 3 Needle image reconstruction in standard B-mode ultrasound image from raw RF data based on envelope detection.

Apparently, this standard technique of signal envelope detection does not fully accommodate the unique characteristics of the acoustic reflection from the needle, where the total backscattered pressure field consists of resonance and non-resonance components, as explained elaborately in Section 4. This phenomenon is affected by several physical parameters that do not interact with each other simultaneously in a simple way, resulting in unique behavior of needle visibility.

The behavior of the backscattered signal from this standard backscattered signal parameter in the time domain based on the signal envelope, particularly around critical incident angles, were observed by plotting the maximum intensity of the signal envelope as a function of the insertion angle. The values in between the discrete insertion angles were obtained by interpolation. Then, this trend was compared to the spectrum of the backscattered pressure field from the simulation.

3.2 Backscattered Signal Parameters in the Frequency Domain

In this research, besides the standard backscattered signal parameter in the time domain based on the signal envelope, the raw RF data were also processed in the frequency domain. The digitization process of acquired signal $x(t)$ from the transducer involved an analog to digital converter (ADC) to convert $x(t)$ to $x(k)$ in discrete domain k. In the measurement, the digital oscilloscope had a sampling frequency of 100 MHz, which is more than 50 times the center frequency of 1.87 MHz, complying with the Nyquist theorem to maintain information content while avoiding aliasing.

$x(k)$ was converted into power spectral density (PSD) by applying Fourier transform with periodogram Welch estimation by returning the one-sided Welch PSD estimation at the specified frequencies f_k and the sampling frequency. This spectrum describes the information about the power of a signal in the frequency domain over the range of observed frequencies. Welch's estimation is performed by dividing the data into overlapping segments. Suppose the data $x(0), x(1), \dots, x(N-1)$ are divided into P segments with length D. They overlap with one another so that one segment of the next segment is displaced along S data ($S \leq D$). Thus, the maximum $P = \frac{N-D}{S} + 1$. The obtained data are in Eq. (5):

$$x^{(p)}(k) = w(k)x(k + pS), 0 \leq k \leq D - 1 \tag{5}$$

where, $0 \leq p \leq P-1$. From those data, the following Eq. (6) is obtained:

$$\tilde{P}_{xx}{}^{(p)}(f_k) = \frac{1}{UDT}\left|X^{(p)}(f_k)\right|^2 \tag{6}$$

At a frequency range of $0 \leq f_k \leq 1/2T$, where T is the period and gives Eqs. (7) and (8) as follows:

$$X^{(p)}(f_k) = T\sum_{k=0}^{D-1} x^{(p)}(k)\exp(-i2\pi f_k kT) \tag{7}$$

$$U = T\sum_{k=0}^{D-1} w^2(k) \tag{8}$$

Eventually, the PSD estimation is given by Eq. (9) as follows:

$$PSD_W(f_k) = \frac{1}{P}\sum_{p=0}^{P-1} \tilde{P}_{xx}^{(p)}(f_k) \tag{9}$$

To observe the energy information contained in the scattered signal, besides the PSD, the energy spectral density (ESD) is extracted by calculating the area under the curve of the PSD with trapezoidal numerical integration.

$$ESD = \sum_0^{f_k} PSD_W(f_k) df_k \tag{10}$$

Similar to the standard backscattered signal parameter in the time domain, the backscattered signal parameters in the frequency domain represented by maximum PSD and ESD were also plotted as a function of the insertion angle to observe their behavior, particularly around the critical incident angles. The values in between the discrete insertion angles were obtained by interpolation. Then, this trend was compared to the spectrum of the backscattered pressure field from the simulation.

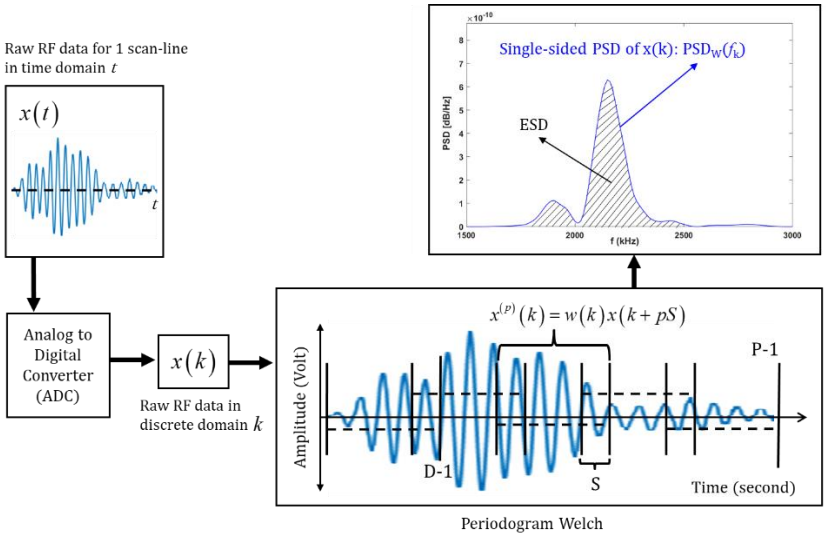

Figure 4 Conversion process from raw RF data $x(t)$ in the time domain to single sided power spectral density (PSD) and energy spectral density (ESD) in the frequency domain.

4 Resonance Scattering Model

The propagation of acoustic wave through an isotropic cylinder must satisfy the governing equations in Eqs. (11) and (12) [21]:

$$\nabla^2\phi = \frac{1}{{c_L}^2}\frac{\partial^2\phi}{\partial t^2} \tag{11}$$

$$\nabla^2 \boldsymbol{\Psi} = \frac{1}{{c_T}^2} \frac{\partial^2 \boldsymbol{\Psi}}{\partial t^2} \tag{12}$$

where ϕ represents the scalar potential and $\boldsymbol{\Psi}$ represents the vector potential. The solutions of these governing equations are solved in each domain involved in the system with the corresponding boundary conditions.

In this case, the incident waves at angle α are assumed to be plane waves insonifying the needle with outer radius a and inner radius b as in Eq. (13)[22]:

$$P_i = P_0 \sum_{n=0}^{\infty} \epsilon_n \, i^n J_n(k_\perp r) \cos(n\theta) \exp[i(k_z z - \omega t)] \tag{13}$$

The geometry of the needle as an infinite hollow cylinder insonified by plane waves is illustrated in Figure 5. Here, P_i is a plane compressional wave that hits the surface of the needle and interacts with its material, P_0 is the pressure amplitude of the incident wave, ϵ_n is the Neumann factor ($\epsilon_0 = 1$ and $\epsilon_n = 2$ for $n \geq 1$), n is the order number, and J_n is a Bessel function of the first kind. k states the wave number, where $k = \omega/c$, $k_\perp = k\, cos\alpha$, $k_z = k\, sin\alpha$. Eq. (13) deals with the solution of wave Eq. (11), which is a component of a longitudinal wave. The backscattered pressure field can be stated as in Eq. (14) follows [22]:

$$P_s = P_0 \sum_{n=0}^{\infty} \epsilon_n \, i^n g_n H_n^{(1)}(k_\perp r) \cos(n\theta) \exp[i(k_z z - \omega t)] \tag{14}$$

where g_n is the scattering coefficient and $H_n^{(1)}$ is a Hankel function of the first kind. To calculate the scattering coefficient g_n, the field is represented by the solutions of the governing equations, i.e. 3 scalar potentials and 1 vector potential in 3 domains (outside cylinder (water), in cylindrical shell (stainless steel), and inside cylinder (air)). g_n as one of the eight unknown coefficients can be found by substituting the solutions of the governing equations into corresponding boundary conditions at the interface of the domains, i.e. $r = a$ and $r = b$, building a system of 8 linear homogeneous equations. As the boundary conditions, the tangential and the shear stresses have to be zero, while the radial stresses and the radial displacement have to be continuous, as explained elaborately by Leon, *et al.* [22].

For this particular phenomenon, the resonance scattering theory was used to calculate the total backscattered pressure field from the needle. The total backscattered pressure field consists of two components, i.e. resonance and non-resonance components [23]. This non-resonance, or rigid background, as if the cylinder is impenetrable, is quite dominant at incident angles approaching 0° in the form of specular reflection from the surface of the needle [15, 16]. When the incident wave hits the surface of the needle in a normal direction, the Rayleigh wave and whispering gallery waves are excited [24]. These waves will travel along the cylinder clockwise and in the opposite direction and will generate resonance if interferences occur constructively among them.

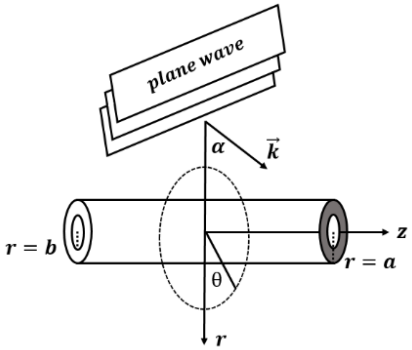

Figure 5 The geometry of an infinite hollow cylinder in the resonance scattering model.

This condition is met only at frequencies where the wavelength of the traveling wave components are related to the physical dimensions of the cylinder. These frequencies are natural frequencies, which define the vibratory response of the cylinder after the initial forcing deformation [25]. In addition to that, at incident angle $\alpha \geq 0$ the axially guided waves will also be excited and generate extra resonance modes [15, 16, 24].

4.1 Resonance Scattering Simulation

In this research, the needle was modeled as an infinite hollow cylinder. As in the measurement, the simulation was carried out for a 22G spinal needle (outer radius a = 0.72 mm, inner radius b = 0.41 mm), and for order number n = 1. The range of the transmit frequency was adjusted around the optimal transmit frequency 1.87 MHz in the measurement, i.e. 0 to 4 MHz. Meanwhile, the incident angle was varied between 0° and 45°, representing the angle of an ultrasonic beam insonifying the needle. As background medium, the needle was surrounded by water that was assumed to be homogeneous and anechoic. The needle itself was stainless-steel type 316, with Young's modulus E is 200 GPa, shear modulus μ is 78.14 GPa, density ρ is 8027 kg/m^3, longitudinal velocity c_L is 5664 m/s, and transversal velocity c_T is 3120 m/s. The needle has two critical angles of incident that identify the generation of certain circumferential waves. These critical angles are formulated as in Eqs. (15) and (16) as follows:

$$\alpha_L = \sin^{-1}\left({c_w} \Big/ \sqrt{{E}/{\rho}} \right) \tag{15}$$

$$\alpha_T = \sin^{-1}\left(\frac{c_w}{\sqrt{\mu/\rho}}\right) \tag{16}$$

c_w= 1492 m/s is the speed of sound in water. The first resonance mode related to the whispering gallery waves can be excited up to the first critical angle, α_L. The second resonance mode can be excited up to the second critical angle, α_T, and caused by the helical guided waves [22]. These two critical incident angles characterize the generation of resonance components when the incident angles are not beneficial anymore for the possibility of generation of non-resonance components from specular reflection. In this case, α_L= 17.4° and α_T= 27.8°. This unique characteristic of acoustic reflection from the needle, where the total backscattered pressure field consists of resonance and non-resonance components is affected by physical parameters, i.e. the frequency of the ultrasound wave, the incident angle of the ultrasound beam to the needle, and the dimensions of the needle. The spectrum of the backscattered pressure field from the simulation was compared by observing the behavior of the backscattered signal parameters from the measurement, particularly around the critical incident angles.

5 Comparison between the Resonance Scattering Model and the Backscattered Signal Parameters

In this research, the resonance scattering model from the simulation was compared to the backscattered signal parameters from the measurement. In this case, the resonance scattering model was taken as standard reference due to its idealized assumptions. The raw RF data from the measurement were processed in the time and the frequency domain to find the most suitable reconstruction method to represent unique information of the total backpropagation from the needle compared to the resonance scattering model. A summary of the comparison of these two models is shown in Table 1.

Table 1 Comparison between backscattered signal parameters and resonance scattering model.

Notes	Backscattered signal parameters (measurement)	Resonance scattering model (simulation)
Backscattered signal equation	Eq. (1)	Eq. (14)
Amplitude Phase	$A(t)$ $\varphi(t)$	g_n $\exp[i(k_z z - \omega t)]$
Represented parameters	$y_{envelope}$ Maximum Power Spectral Density (PSD) Energy Spectral Density (ESD)	Backscattered pressure field with fractional bandwidth: $P_S(BW, \alpha)$

5.1 Random Characteristics of the Backscattered Signal

The ultrasound wave interacts with each scatterer, resulting in its own backscattered echo, i.e. a sinusoidal wave with a phase and amplitude change. The individual amplitudes $\{a_n\}$ and phases $\{\varphi_n\}$ of the scatterers are not directly observable because of their small scale as compared to the wavelength [19]. The received signal $\boldsymbol{A}$ consists of the superposition of all the phases and amplitudes from each scatterer as in Eq. (17) [26, 27]:

$$\boldsymbol{A} = A.e^{i\theta} = \frac{1}{\sqrt{N}}\sum_{n=1}^{N} a_n = \frac{1}{\sqrt{N}}\sum_{n=1}^{N} a_n e^{i\varphi_n} \tag{17}$$

where a_n is the n^{th} of N phasor components with associated length a_n and phase φ_n. In this case, $\frac{1}{\sqrt{N}}$ is a normalization constant needed to preserve the second-order moment [26]. The signal $\boldsymbol{A}$ is a complex random phasor, where in the signal acquisition process only its real component is acquired by the transducer, i.e. in Eq. (18) as follows:

$$X = Re\{\boldsymbol{A}\} = \frac{1}{\sqrt{N}}\sum_{n=1}^{N} a_n cos\varphi_n \tag{18}$$

Since the interference between a diffuse collection of scatterers can be constructive or destructive, the observed signal contains randomness in the phase [28, 29]. This process of interference itself is deterministic, but because of the permanent change in interference it leads to observable spatial randomness [19].

5.2 Fractional Bandwidth of the Backscattered Pressure Field from the Resonance Scattering Model

In comparison with the random characteristics of the backscattered signal from the measurements, the spectrum of the backscattered pressure field from the simulation was extracted with 10% to 100% fractional bandwidth centered at frequency f_C = 1.87 MHz. At the center frequency, the spectrum of the backscattered pressure field represents the backscattered pressure field as a function of frequency and incident angle ($P_S(f, \alpha)$).

The center frequency and bandwidth are related to the tradeoffs in the signal-to-noise ratio and the spatial resolution. There is no general understanding about the optimal parameters for a specific application [30]. The optimal fractional bandwidth was chosen by comparing the fractional bandwidths to the distribution of the signal parameters from the measurements. In this case, the distribution of the backscattered pressure field representing the RF data from the simulation was modeled by a Gaussian distribution. The spectrum at discrete incident angles of 0° to 45° (resolution = 5°) was weighted by a Gaussian window characterized by 10% to 100% fractional bandwidth. The coefficients of the Gaussian window were calculated with this equation:

$$w_G(n) = e^{-0.5\left(\alpha\frac{n}{\frac{N-1}{2}}\right)^2} = e^{-n^2/2\sigma^2} \tag{19}$$

where $-(N-1)/2 \leq n \leq (N-1)/2$ and α is inversely proportional to standard deviation σ of a Gaussian random variable. The exact correspondence with the standard deviation of the Gaussian probability density function is $\sigma = (N-1)/(2\alpha)$. The fractional bandwidth characterizes the width of the band of the pulse centered at f_C (See Eqs. (20) and (21))

$$Fractional\ Bandwidth\,(\%) = \frac{f_H - f_L}{f_C} \tag{20}$$

$$f_C = (f_H + f_L)/2 \tag{21}$$

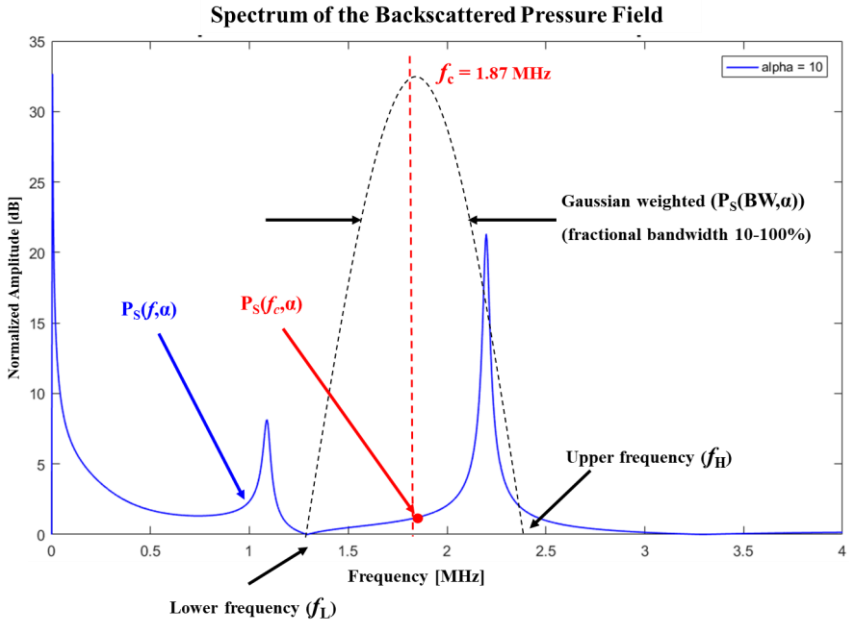

Figure 6 Gaussian weighting (10-100% fractional bandwidth) centered at f_C =1.87 MHz for the spectrum of the backscattered pressure field at incident angle α =10°.

At one point of the incident angles, a single value of the mean amplitude is obtained after being weighted by the Gaussian window. Figure 6 shows the example of Gaussian weighting for the spectrum of the backscattered pressure field at incident angle α = 10°.

The weighted spectrum represents the backscattered pressure field as a function of bandwidth frequency and incident angle ($P_S(BW, \alpha)$).

6 Results and Discussion

The comparison between the backscattered signal parameters from the measurements and the resonance scattering model from the simulation was focused particularly on the behavior of the backscattered signal around the critical incident angles (α_L= 17.4° and α_T= 27.8°). Around these critical angles, the acoustic scattering from the needle is unique compared to common acoustic scattering from tissue, which is characterized by the addition of a resonance component to the total backpropagation.

6.1 Measurement Result of the Backscattered Signal Parameters

The three signal parameters as reconstruction methods for needles in B-mode ultrasound images, i.e. signal envelope ($y_{envelope}$), maximum PSD, and ESD were plotted over a range of insertion angles of 0° to 45°. These reconstruction methods were performed per single A-mode scan-line to represent the backscattered pressure field. Here, the insertion angle was assumed to represent the incident angle of the ultrasound beam to the needle because no effect of beam forming was included in the measurement. Based on its material properties, the needle has two critical incident angles, i.e. α_L= 17.4° and α_T= 27.8°.

It can be observed from Figure 7 that the maximum intensity of the signal envelope, maximum PSD and ESD, were highest at α = 0°. This shows that the most dominant backpropagation is from specular reflection from the surface of the needle (non-resonance component), where the ultrasonic beam hits and is reflected perpendicular to the needle.

Furthermore, these three signal parameters decrease drastically at α = 5°. This tendency is due to the backpropagation from specular reflection becoming less dominant than at α = 0°. Then, it gradually increases until $\alpha \approx$ 30°, except for the maximum intensity of the signal envelope. Within this range, there are two critical angles α_L = 17.4° and α_T = 27.8° that cause an increase of backpropagation from resonance scattering (resonance component). After that, they decrease in a relatively stable manner because it is away from the region of the critical angles along with the increase of the transmit-receive distance from the transducer.

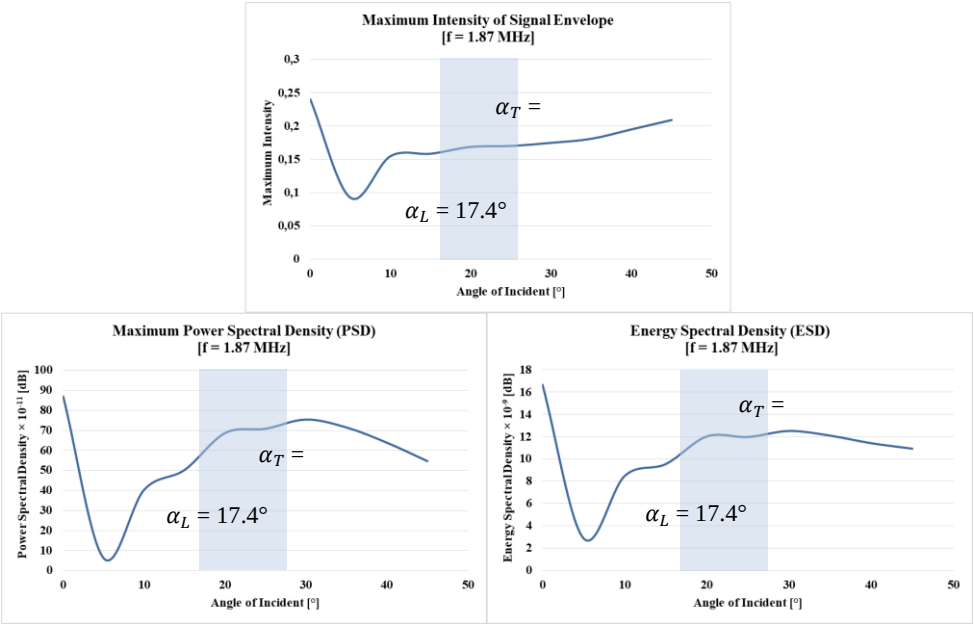

Figure 7 The distribution of three signal parameters as reconstruction method of the backscattered signal from measurement: maximum intensity of signal envelope, maximum PSD, and ESD.

The effect of the resonance scattering on the total backpropagation around the range of critical incident angles could be observed more clearly in the signal parameters in the frequency domain, i.e. maximum PSD and ESD. These distributions were then compared to the simulation results to confirm the same effect.

6.2 Simulation Result of the Resonance Scattering Model

The spectrum of the backscattered pressure field for a 22G spinal needle was plotted in a frequency range of 0 to 4 MHz, close to the optimal transmit frequency of 1.87 MHz as in the measurement (see red line in Figure 8). To accommodate the random characteristic of the RF data, the spectrum of the backscattered pressure field was extracted with 10% to 100% fractional bandwidth centered at f_C = 1.87 MHz.

The spectrum at discrete incident angles of 0° to 45° (resolution = 5°) were weighted by a Gaussian window characterized by 10% to 100% fractional bandwidth and plotted as a function of the incident angle (see Figure 9). The values in between the discrete incident angles were obtained by interpolation. In

this case, the optimal fractional bandwidth was chosen by comparing it to the distribution of the signal parameters from the measurements.

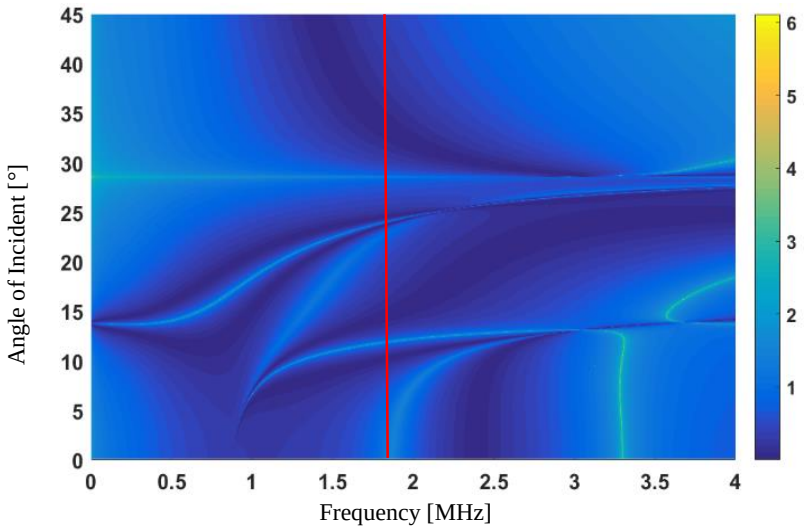

Figure 8 Spectrum of the backscattered pressure field of a 22G spinal needle from the simulation over the range of incident angles $\alpha = 0° - 45°$.

Comparing Figure 9 to Figure 7, the fractional bandwidth was relatively optimal at 40% to 100% bandwidth. Within this range, the trend of the backscattered signal was more similar to the distribution of the signal parameters in the frequency domain from the measurements, i.e. maximum PSD and ESD (see the particular trend around the critical angles in Figures 7 and 9). So that the simulation of the resonance scattering model can be used to predict the backscattered response from the needle, it must be able to confirm it to the real conditions of RF data with random characteristics. Therefore, the extraction of the backscattered pressure field in the simulation with fractional bandwidth should be a concern.

From this comparison, it is not expected that they will be similar in absolute values because the conditions in the simulation were assumed to be ideal and different from the conditions in the measurements, i.e. the difference in the exact values of acoustic parameters of the needle and the background medium, the width of the transmit and echo signals in the measurements were not ideal, while in the simulation the transmit wave was assumed to be a plane wave. In addition, the small changes in the positioning of the transducer and the needle in the measurements also affected the results. Furthermore, in the simulation the attenuation of the background medium was ignored.

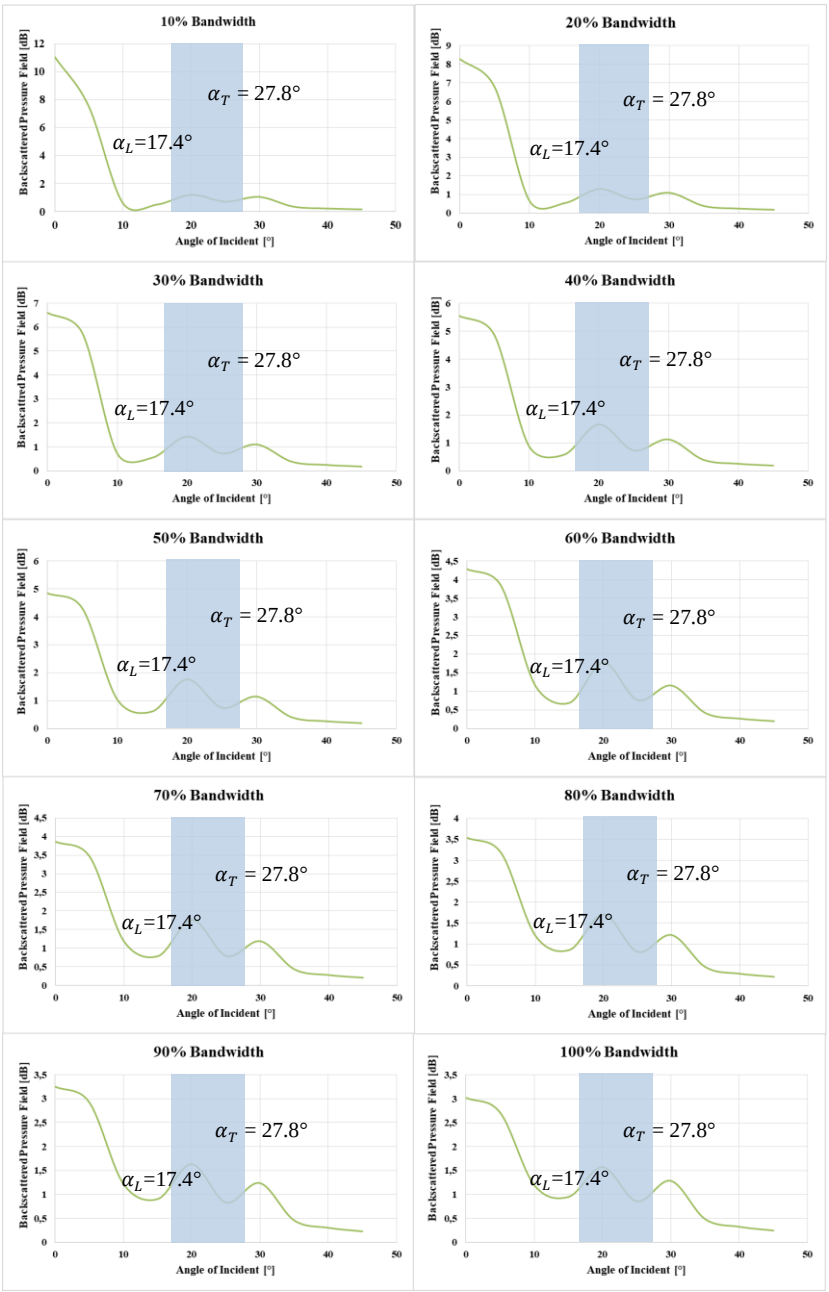

Figure 9 Spectrum of the backscattered pressure field of a 22G spinal needle from the simulation over the range of incident angles α = 0°−45°, with 10−100% fractional bandwidth.

7 Conclusion

The measurements with a center frequency of 1.87 MHz confirmed that the effect of the resonance scattering on the total backpropagation around the critical incident angles was observed more clearly at maximum PSD and ESD. On the other hand, it could not be observed clearly by standard B-mode ultrasound image reconstruction based on the A-mode signal envelope. In this specific case of needle image reconstruction, these parameters (maximum PSD and ESD) are more representative because they contain unique information of the total power and energy of the backscattered signal from the needle, which consist of non-resonance and resonance scattering components. From these findings, it is recommended that the reconstruction of needle images should be derived from maximum PSD and ESD to optimize the contrast of the needle in B-mode ultrasound images.

From the simulation result, the fractional bandwidth of the spectrum of the backscattered pressure field was relatively optimal at 40% to 100% bandwidth centered at f_C = 1.87 MHz. So that the simulation of the resonance scattering model can be used to predict the backscattered response from the needle, it must be able to confirm it to the real conditions of RF data with random characteristics. Therefore, the extraction of the backscattered pressure field in the simulation with a fractional bandwidth should be a concern.

Acknowledgements

We acknowledge the Indonesia Endowment Fund for Education (LPDP) for providing a scholarship for this doctoral research and the Ministry of Education and Culture of Republic of Indonesia for its competency-based research funding.

References

[1] Nichols, K., Wright, L.B., Spencer, T. & Culp, W.C., *Changes in Ultrasonographic Echogenicity and Visibility of Needles with Changes in Angles of Insonation*, J. Vasc. Interv Radiol., **14**, pp. 1553-1557, 2003.

[2] de Korte, C.L., Weijers, G., Vriezema, D.M., Keereweer, A.R., Thijssen, J.M. & Hansen, H.H.G., *Quantitative Analysis of Coated Needles for Ultrasound Guided Intervention*. Proc IEEE International Ultrasonics Symposium, pp. 1571-1574, 2015.

[3] Culp, W.C., McCowan, T.C., Goertzen, T.C., Habbe, T.G., Hummel, M.M., LeVeen, R.F. & Anderson, J.C., *Relative Ultrasonographic Echogenicity of Standard, Dimpled, and Polymeric-Coated Needles*. J Vasc Interv Radiol, **11**, pp. 351-358, 2000.

[4] de Jong, T.L., van de Berg, N.J., Tas, L., Dankelman, J. & van den Dobbelsteen, J.J., *Needle Placement Errors. Do We Need Steerable Needles in Interventional Radiology?* Med Devices Evidence Res, **11**, pp. 259-265, 2018.

[5] Chin, K.J., Perlas, A., Chan, V.W.S. & Brull, R., *Needle Visualization in Ultrasound-Guided Regional Anesthesia: Challenges and Solutions*, Reg Anes Pain Med, **33**(6), pp. 532-544, 2008.

[6] Schafhalter-Zoppoth, I., McCulloch, C.E. & Gray, A.T., *Ultrasound Visibility of Needles Used for Regional Nerve Block: An In Vitro Study*, Reg Anes Pain Med., **29**(5), pp. 480-488, 2004.

[7] Maecken, T., Zenz, M. & Grau, T., *Ultrasound Characteristics of needles for Regional Anesthesia*, Reg Anes Pain Med, **32**(5), pp. 440-447, 2007.

[8] Susanti, H., Suprijanto, & Kurniadi, D., *A Quantification System of Needle Visibility in B-Mode Ultrasound with Linear and Curved Transducer*, International Journal of Biology and Biomedical Engineeering, **14**, pp. 12-20, 2020.

[9] Susanti, H., Suprijanto, & Kurniadi, D., *Two-Dimensional Mapping of Needle Visibility with Linear and Curved Array for Ultrasound-Guided Interventional Procedure*, AIP Conference Proceedings, **1933**, pp. 040004, 2018.

[10] Rumble, S., Schmitz, G. & Dencks, S., *Sonographic Visibility of Cannulas using Convex Ultrasound Transducers*, Biomed. Tech., **64**(6), pp. 691-698, 2019.

[11] Brookes, J., Sondekoppam, R., Armstrong, K., Uppal, V., Dhir, S., Terlecki, M. & Ganapathy, S., *Comparative Evaluation of the Visibility and Block Characteristics of a Stimulating Needle and Catheter vs an Echogenic Needle and Catheter for Sciatic Nerve Block with a Low-frequency Ultrasound Probe*, British Journal of Regional Anaesthesia, **115**(6), pp. 912-919, 2015.

[12] Buonsenso, D., Pata, D. & Chiaretti, A., *COVID-19 Outbreak: Less Stethoscope, More Ultrasound*, Lancet Respir Med, **8**(5), pp. e27, 2020.

[13] Buonsenso, D., Piano, A., Raffaelli, F., Bonadia, N., De Gaetano Donati, K. & Franceschi, F. *Point-of-Care Lung Ultrasound Findings in Novel Coronavirus Disease-19 Pnemoniae: A Case Report and Potential Applications during COVID-19 Outbreak*, European Review for Medical Pharmacological Sciences, **24**, pp.2776-2780, 2020.

[14] Peng, Q.Y., Wang, X.T., Zhang, L.N. & Chinese Critical Care Ultrasound Study Group, *Findings of Lung Ultrasonography of Novel Corona Virus Pneumonia during the 2019-2020 Epidemic*, Intensive Care Med., **46**, pp. 849-850, 2020.

[15] Dencks, S. & Schmitz, G., *Assessment of the Potential of Beamforming for Needle Enhancement in Punctures*, Proc IEEE International Ultrasonics Symposium, pp. 1-4, 2015.

[16] Dencks, S., Susanti, H. & Schmitz, G., *Needle Visibility for Deep Punctures with Curved Arrays*, Proc IEEE International Ultrasonics Symposium, pp. 1880-1883, 2014.
[17] Shiavi, R., *Introduction to Applied Statistical Signal Analysis: Guide to Biomedical and Electrical Engineering Applications, 3rd ed.*, Burlington, MA, Academic Press, 2007.
[18] Oppenheim, A. & Schafer, R. *Discrete-time Signal Processing*, Upper Saddle River, New Jersey, Prentice Hall, 2010.
[19] Klein, T.J. *Statistical Image Processing of Medical Ultrasound Radio Frequency Data*, Doctoral Dissertation, Technical University of Munich, 2012.
[20] Misaridis, T. *Ultrasound Imaging using Coded Signals*, Doctoral Dissertation, Technical University of Denmark, 2001.
[21] Pollard, H.F., *Resonant Behaviour of an Acoustical Transmission Line*, Australian Journal of Physics, **15,** pp. 513-526, 1962.
[22] Leon, F., Lecroq, F., Decultot, D. & Maze, G., *Scattering of an Obliquely Incident Wave by an Infinite Hollow Cylindrical Shell*, Journal Acoustical Society of America, **91**(3), pp. 1388-1397, 1992.
[23] Fan, Y., Honarvar, F., Sinclair, A.N. & Jafari, M-R. *Circumferential Resonance Modes of Solid Elastic Cylinders Excited by Obliquely Incident Acoustic Waves*, Journal Acoustical Society of America, **113**(1), pp. 102-113, 2003.
[24] Flax, L., Dragonette, L.R. & Überall, H., *Theory of Elastic Resonance Excitation by Sound Scattering*, Journal Acoustical Society of America, **63**(3), pp. 723-731, 1978.
[25] Lesage, J. *Nondestructive Evaluation of Pre-stressed Concrete Cylinder Pipe by Resonance Acoustic Spectroscopy: Theoretical and Modelling Considerations*, Doctoral Dissertation, University of Toronto, 2015.
[26] Goodman, J., *Speckle Phenomena in Optics: Theory and Applications*, Englewood, Colorado, Roberts, and Company Publishers, 2007.
[27] Dutt, V., *Statistical Analysis of Ultrasound Echo Envelope*, PhD Thesis, Mayo Graduate School, 1995.
[28] Soergel, U. *Radar Remote Sensing of Urban Area*, Springer, 2010.
[29] Wagner, R.F., Insana, M.F. & Brown, D.G., *Statistical Properties of Radiofrequency and Envelope Detected Signals with Applications to Medical Ultrasound*, J. Opt. Soc. Am., **4**(5), pp. 910-922, 1987.
[30] Abbey, C.K., Nguyen, N.Q. & Insana, M.F., *Effect of Frequency and Bandwidth on Diagnostic Information Transfer in Ultrasonic B-mode Imaging*, IEEE Trans Ultrason Ferroelectr Freq Control, **59**(6), pp. 1115-1126, 2012.